Emergent anomalous hydrodynamics at infinite temperature in a long-range XXZ model

Ang Yang, Jin-Lou Ma,* and Lei Ying†
School of Physics, Zhejiang Key Laboratory of Micro-nano Quantum Chips and Quantum Control, Zhejiang University, Hangzhou 310027, China

(Received 25 March 2024; revised 3 July 2024; accepted 3 July 2024; published 16 July 2024)

The conventional wisdom suggests that transports of conserved quantities in nonintegrable quantum many-body systems at high temperatures are diffusive. Recent study suggests a potential counterexample of this paradigm. We independently complement this counterexample by directly uncovering anomalous infinite-temperature hydrodynamics in a spin-1/2 XXZ chain with power-law couplings. This model, classified as nonintegrable due to its Wigner-Dyson level-spacing statistics in the random matrix theory, exhibits a surprising superdiffusive-ballistic-superdiffusive transport transition by varying the power-law exponent of couplings for a fixed anisotropy. Our findings are verified by multiple observables, including the spin-spin autocorrelator, mean-square displacement, and spin conductivity. Interestingly, we further quantify the degree of quantum chaos using the Kullback-Leibler divergence between the entanglement entropy distributions of the model's eigenstates and a random state. Remarkably, an observed local maximum in the divergence near the transition boundary suggests a link between anomalous hydrodynamics and a suppression of quantum chaos. This work offers another deep understanding of emergent anomalous transport phenomena in a wider range of nonintegrable quantum many-body systems.

DOI: 10.1103/PhysRevB.110.014308

I. INTRODUCTION

Recently, probing the emergent hydrodynamics with a few conserved quantities in quantum many-body systems has attracted wide interest in both experimental and theoretical communities [1–12]. In general, ballistic transport is considered to mostly occur in integrable quantum many-body systems despite some counterexamples. These systems have stable quasiparticles that propagate without scattering, leading to ballistic transport, while the standard diffusion is expected for nonintegrable systems [12]. However, recent works have revealed that both integrable and nonintegrable models can exhibit unusual late-time transports with different mechanisms [8,12–21]. On the experimental side, associated with the great development of various quantum simulators, in particular such as cold atoms in optical lattices [3,22–26], Rydberg atoms [27–33], superconducting processors [34], and ion traps [1,35–38], a broad class of transport behavior has been observed.

Among them, the Heisenberg spin system is an important platform to study various quantum transport behaviors at infinite temperature, such as in 1D spin-1/2 chains [2,6,17,19,39], ladders [40,41], and 2D lattices [3]. The coupling range and type of spin exchange can govern integrability and transport in quantum many-body systems. For example, in the paradigmatic spin-1/2 XXZ chain, the isotropic point $\Delta = 1.0$ exhibits Kardar-Parisi-Zhang (KPZ) superdiffusion [9,11,12]. Standard diffusion recovers at $\Delta > 1.0$, while ballistic transport prevails for $\Delta < 1.0$, as expected for integrable models [3,6,9,11,12,17,18,39]. On the other hand, long-range interactions are ubiquitous in atomic and ion-trapping systems, encompassing a diverse range of types [42–46], and many recent works have focused on the properties of these interactions in long-range models, such as localization [47–49], bound states [50,51], nonlocality and entanglement [52–60], etc. Interestingly, the spin-1/2 XY chain with power-law couplings, despite being a nonintegrable model, exhibits anomalous hydrodynamics. This behavior corresponds to classical Lévy flights, distinguishing from the traditional diffusion [1–3,9,61]. Traditionally, studies of spin models have investigated the independent effects of anisotropy and long-range couplings, both of which can induce anomalous transport behaviors. However, these anomalous transports arise from distinct mechanisms and monotonically speed up or slow down as relevant parameters change. Hence, a key question remains: What kind of transport will emerge from the interplay between anisotropy and long-range couplings? More importantly, what signatures characterize these anomalous hydrodynamics, in particular in nonintegrable models? One intriguing possibility is the appearance of nonmonotonic transitions. Previous work in Ref. [20] explored spin transport in a long-range isotropic Heisenberg model with disorders, finding subdiffusion. However, the effects of anisotropy and long-range couplings were suppressed due to the dominant disorder. In Ref. [62], Mierzejewski *et al.* independently investigated a long-range anisotropic Heisenberg model without disorders, finding quasiballistic transport and nonmonotonic behavior. They studied the spin conductivity in a Hilbert subspace, discovering a long line in the parameter space where

*Contact author: 0622668@zju.edu.cn
†Contact author: leiying@zju.edu.cn

quasiballistic transports exist, consistent with their domain-wall expansion analysis.

To address these questions, in this paper, we utilize the spin-spin autocorrelation function to directly investigate the magnetization dynamics across the entire Hilbert space at infinite temperature. This is a theoretically straightforward and well-known approach to probe infinite-temperature transports [1,2,6,19,39]. In a long-range clean spin-1/2 XXZ model, this approach allows us to quantitatively extract the dynamical exponent to distinguish different transport regimes. Our further analysis based on the eigenstates' entanglement entropy of the system provides a new correspondence between anomalous transports and the system's ability against quantum chaos. The paper is organized as follows. The model and observables are first introduced in Sec. II. In Sec. III, we describe in detail the relevant numerical methods, i.e., dynamical quantum typicality (DQT) and the time-dependent variational principle (TDVP). The numerical results based on different observables are presented and discussed in Sec. IV.

II. MODELS AND OBSERVABLES

We investigate the magnetization dynamics of a one-dimensional clean and undriven spin-1/2 XXZ chain with power-law couplings. The system is subjected to a magnetic field applied along the z axis [63]. Under open boundary conditions, the Hamiltonian of the system can be written as

$$\hat{H} = \frac{1}{\mathcal{N}} \sum_{i<j}^{L} \frac{-J}{|i-j|^{\alpha}} \left(\hat{\sigma}_i^x \hat{\sigma}_j^x + \hat{\sigma}_i^y \hat{\sigma}_j^y + \Delta \hat{\sigma}_i^z \hat{\sigma}_j^z\right) + h_z \sum_{i=1}^{L} \hat{\sigma}_i^z, \tag{1}$$

where $\hat{\sigma}_i^{\mu}$, $\mu \in \{x, y, z\}$, are the standard spin-1/2 Pauli matrices of site i. L, J, and h_z denote the system size, the coupling strength, and the magnetic field, respectively. $\Delta > 0$ is the ferromagnetic anisotropy along the z direction, and the parameter α determines the strength of the long-range couplings between arbitrary sites in the chain. Here we introduce the Kac norm $\mathcal{N} = \sum_{i<j} |i-j|^{-\alpha}/(L-1)$ and it rescales the Hamiltonian to eliminate its dependence on the system size L and the coupling parameter α. This ensures that the energy density has the correct scaling behavior, independent of system size [2,63]. The anisotropy parameter Δ breaks a symmetry in the rotating frame. In the isotropic case, $\Delta = 1$ with both $U(1)$ and $SU(2)$ symmetries unbroken as well as the total $\vec{\sigma}$ conserved; in the presence of axial anisotropy along the z axis, $\Delta \neq 1$ with $U(1)$ symmetry unbroken and the total σ^z magnetization conserved. These conserved quantities determine the macroscopic late-time hydrodynamics of the quantum system. In the rest of this paper, we always keep $J = 1$ which sets the time unit, as well as magnetic field at a fixed value $h_z = 3$ [63].

In general, the transport property can be directly measured by observing how a single spin excitation scatters against a background at an infinite temperature [1,2]. In detail, we initiate a spin excitation at the center of the chain at time $t = 0$ by applying $\hat{\sigma}_0^z$. Then, we track its propagation through space and time by obtaining the unequal-time correlation function at infinite temperature [1], which is given by

$$C_j(t) = \left\langle \hat{\sigma}_j^z(t) \hat{\sigma}_0^z(0) \right\rangle_{T=\infty}, \tag{2}$$

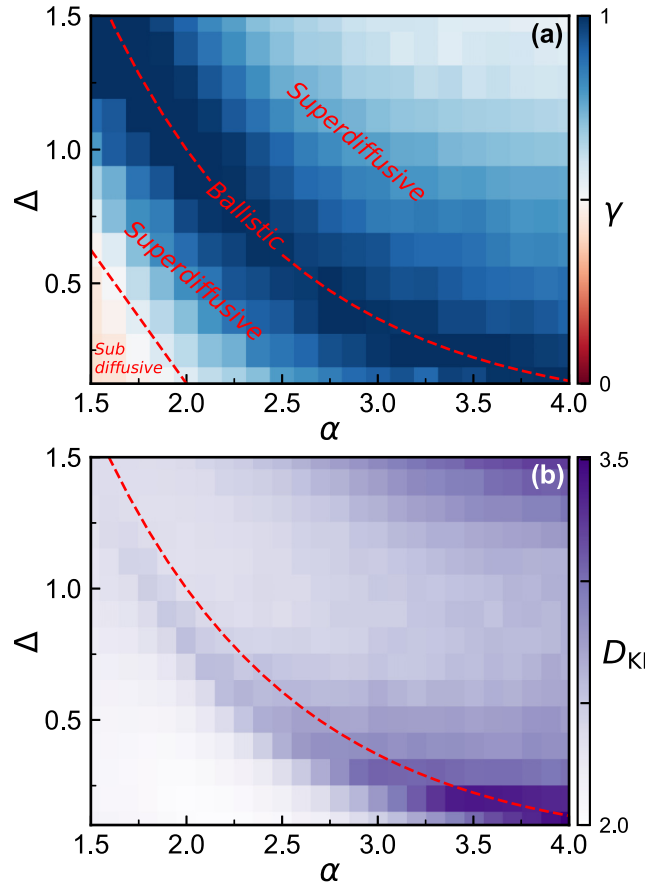

FIG. 1. (a) Dynamical exponent γ extracted from the autocorrelator $C_0(t)$ as a function of Δ and α. The numerical results are obtained by the DQT method with $L = 21$. The ballistic transport (the darkest blue) corresponds to $\gamma \sim 1$ and the red region denotes subdiffusion ($0 < \gamma < 1/2$), while superdiffusion ($1/2 < \gamma < 1$) dominates in the light blue region. The red dashed line (lower left) marks the boundary between superdiffusive and subdiffusive regimes. (b) The logarithm of Kullback-Leibler (KL) divergence between the microcanonical distribution of eigenstate EE and the Bianchi-Dona (BD) distribution. The system size for panel (b) is $L = 14$ with the half-filling condition. The red dashed curve in (a) and (b) is the exponential function $\Delta \simeq e^{-\alpha+2}$.

where $\hat{\sigma}_j^z(t) = e^{i\hat{H}t} \hat{\sigma}_j^z e^{-i\hat{H}t}$ is the time-dependent operator in the Heisenberg picture with an initial condition of $C_0(0) = 1$. In particular, the autocorrelator $C_0(t)$ determines the remaining excitation at the central site and it is expected to exhibit anomalous hydrodynamics, as illustrated in Fig. 1. We will explicitly discuss our results in Sec. IV.

In an isolated quantum many-body system, preparing a state with infinite temperature is challenging. According to the canonical thermal ensemble theory at finite temperature, the equilibrium expectation value of an observable is equivalent to the trace of the product of the density operator and the observable [64]. Thus, we have

$$C_j(t) = \frac{\mathrm{Tr}\left[e^{-\beta\hat{H}} \hat{\sigma}_j^z(t) \hat{\sigma}_0^z(0)\right]}{Z}, \tag{3}$$

where $Z = \mathrm{Tr}[e^{-\beta\hat{H}}]$ is the canonical partition function with the inverse temperature $\beta = 1/T$. Then, we introduce the spatial variance of $C_j(t)$, also known as the mean-square displacement (MSD), given by [20]

$$\Sigma^2(t) = \sum_{j=-L/2}^{L/2} j^2 C_j(t) - \left(\sum_{j=-L/2}^{L/2} j C_j(t) \right)^2, \tag{4}$$

which is directly related to the time-dependent diffusion coefficient $D(t) = d\Sigma^2/2dt$. In the diffusion scenario, $\Sigma(t) \propto t^{1/2}$ and $D(t)$ converge to a constant in the long-time limit. Apart from this, the transport is considered as superdiffusive for $\Sigma(t) \propto t^{\gamma}$ with $\gamma \in (1/2, 1)$, ballistic for $\gamma = 1$, and subdiffusive for $\gamma \in (0, 1/2)$ [9,11,12,17,18,20]. Hence, we define a time-dependent dynamical exponent $\gamma(t) = d \ln \Sigma^2(t)/2d \ln t$ to extract γ. In the thermodynamic limit, the spin autocorrelator is expected to decay following a power law [5], expressed as

$$\lim_{t,L\to\infty} C_0(t) \sim t^{-\gamma}. \tag{5}$$

In practice, Eq. (3) can be expressed as an equally weighted trace over any sets of complete eigenstates, e.g., product states in the σ^z basis [1]. However, it is hard to calculate the trace exactly for a large system as the Hilbert-space dimension is $\mathcal{N} = 2^L$. Hence two approximate numerical methods are exploited in Sec. III.

III. NUMERICAL APPROACHES

A. Dynamical quantum typicality

The dynamical quantum typicality (DQT) indicates that a single pure quantum state can exhibit the same properties of an entire statistical ensemble [6,39,64–66]. It is also effective even in the cases beyond the eigenstate thermalization hypothesis [67,68], and is a powerful tool in general for the accurate calculation of real-time correlation functions [6,64,66,69,70].

The main idea amounts to replacing the trace $\mathrm{Tr}\{\bullet\} = \sum_i \langle i| \bullet |i\rangle$ in Eq. (3) by a simple scalar product $\langle\psi| \bullet |\psi\rangle$. Here, $|\psi\rangle$ is a reference pure state, which is randomly drawn from the Hilbert space according to the unitary invariant Haar measure [66,71]. Then, it allows us to rewrite the unequal-time correlation function in Eq. (3) as [6,69,70,72]

$$C_j(t) = \frac{\mathrm{Re}\langle\psi|e^{-\beta\hat{H}}\hat{\sigma}_j^z(t)\hat{\sigma}_0^z(0)|\psi\rangle}{\langle\psi|e^{-\beta\hat{H}}|\psi\rangle} + \epsilon(|\psi\rangle). \tag{6}$$

At $T \to \infty$, the correlation function can be written as

$$C_j(t) = \frac{\mathrm{Re}\langle\psi(t)|\hat{\sigma}_j^z|\phi(t)\rangle}{\langle\psi(0)|\psi(0)\rangle} + \epsilon(|\psi\rangle), \tag{7}$$

where two auxiliary pure states are given by [73]

$$\begin{aligned} |\psi(t)\rangle &= e^{-i\hat{H}t}|\psi\rangle, \\ |\phi(t)\rangle &= e^{-i\hat{H}t}\hat{\sigma}_0^z|\psi\rangle. \end{aligned} \tag{8}$$

The reference pure state $|\psi\rangle$ is randomly drawn in Hilbert space, as follows [6,74]:

$$|\psi\rangle = \sum_{k=1}^{d} (a_k + ib_k)|k\rangle, \tag{9}$$

where the pure state $|k\rangle$ denotes an arbitrary basis of the Hilbert space and the coefficients a_k and b_k are random real numbers, usually drawn from a Gaussian distribution with zero means (other types of randomness are also available) [6]. Note that the distribution is invariant regardless of any unitary transformations within the Hilbert space. Thus, $|\psi\rangle$ is a good representative of a thermal statistical ensemble and nearly maximally entangled [64,71,75].

In Eq. (7), the first term is an approximation of $C_j(t)$, and the second one $\epsilon(|\psi\rangle)$ is the error which is naturally random because of the random choice of typical state $|\psi\rangle$ [6]. This random error could be eliminated by taking samples over multiple $|\psi\rangle$ [6]. Notably, the standard deviation of the statistical error $\epsilon = \epsilon(|\psi\rangle)$ has an upper bound and scales as $\sigma(\epsilon) \propto 1/\sqrt{d_{\mathrm{eff}}}$, where $d_{\mathrm{eff}} = \mathrm{Tr}\{\exp[-\beta(H - E_0)]\}$ is the effective dimension of the Hilbert space with E_0 being the ground-state energy of H [6,69,71,72]. Also, d_{eff} is the number of thermally occupied states and $d_{\mathrm{eff}} = d$ for $\beta = 0$ [64]. Therefore, the error ϵ exponentially decays with the increase of the system size L. Remarkably, for our case $\beta \to 0$, DQT is a good approximation [6,64].

In this way, the trace operation in Eq. (3) is completely transformed into the time evolution of two auxiliary pure states $|\psi\rangle$ and $\hat{\sigma}_0^z|\psi\rangle$. The full evolution can be subdivided into a product of consecutive steps as [64]

$$|\psi(t)\rangle = (e^{-i\hat{H}\delta t})^N|\psi\rangle, \tag{10}$$

where each step can be evaluated utilizing a Taylor expansion of the exponential $e^{-i\hat{H}\delta t}$ for sufficiently small δt instead of diagonalization. In this paper, we take DQT as a benchmark approach by using an open-source Python package QuSpin [76]. Note that we always consider the entire Hilbert space without any restriction in the context of the DQT method. The number of typical states used in DQT are 5, 2, 1, 1 for system sizes $L = 17, 19, 21, 23$, respectively.

B. Time-dependent variational principle

In addition to the DQT approach, the transport properties can also be investigated utilizing the time-dependent variational principle in the manifold of matrix product states (TDVP-MPS) [19,20,77–79]. The matrix product state method allows us to deal with large spin systems, far beyond the state-of-the-art limit of the exact diagonalization techniques [80]. Moreover, a few macroscopic quantities in the spin chains are explicitly conserved in this method, including the total energy, total magnetization, and total number of particles. For sufficiently large bond dimensions, the method is numerically exact with limitations arising from the growth of entanglement entropy with time, which requires numerical efforts exponentially [81]. Recent studies have shown that it is possible to handle the time evolution problem of long-range systems using TDVP applied to the manifold of MPS [19,20].

A tensor of order N with finite dimension can be expressed as the product of N matrices, and this representation is essentially a decomposition of tensors. Equivalently, a many-body wave function in Hilbert space

$$|\Psi\rangle = \sum_{\{i_n\}=1}^{d} C_{i_1,i_2,\ldots,i_N} |i_1 i_2 \cdots i_N\rangle \tag{11}$$

can be written as a matrix product state

$$|\Psi[A]\rangle = \sum_{\{i_n\}=1}^{d} A^{i_1}(1) A^{i_2}(2) \cdots A^{i_N}(N) |i_1 i_2 \cdots i_N\rangle, \tag{12}$$

where d denotes the local Hilbert space dimension at each site i_n (e.g., $d = 2$ in the spin-1/2 case), $A^{i_n}(n)$ is a complex matrix with a dimension of $D_{n-1} \times D_n$, and the equivalence of Eq. (11) and Eq. (12) naturally leads to $D_0 = D_L = 1$. As the Hilbert space dimension grows exponentially with system size, the dimension (also known as bond dimension) of the matrices $A^{i_n}(n)$ also increases exponentially. However, for many-body wave functions with low entanglement, we can achieve a good approximation using a series of matrices with small dimensions. This is done by truncating the dimension to a fixed size feasible for computation. This approximation is considered accurate when it converges as we increase this truncated dimension [20].

Since the typical pure state $|\psi\rangle$ is nearly maximally entangled, it cannot efficiently be represented as an MPS. Instead, we approximate the trace in Eq. (3) as

$$C_j(t) \approx \frac{1}{N_s} \sum_{i=1}^{N_s} \langle i | \hat{\sigma}_j^z(t) \hat{\sigma}_0^z(0) | i \rangle. \tag{13}$$

To obtain an unbiased average of $C_j(t)$, we sample the product states $|i\rangle$ based on σ^z from a probability distribution where each configuration has an equal probability of being chosen [1]. In practice, it suffices to sample a reasonable number $N_s \approx$ 10–100 of product states to evaluate Eq. (3). To further reduce the statistical noise and improve the convergence of Eq. (13), the conjugate configuration is prepared for each random state, in which all spins except the central one are flipped [1].

The main idea of TDVP is to project the time evolution onto the manifold $\mathcal{M}$ of the variational wave function (precisely MPS). This is equivalent to solving the Schrödinger equation projected onto the tangent space [20,79]

$$i \frac{d|\Psi[A]\rangle}{dt} = P_{\mathcal{M}} \hat{H} |\Psi[A]\rangle, \tag{14}$$

where $P_{\mathcal{M}}$ stands for a projector to the tangent space $\mathcal{M}_\chi$ with fixed bond dimension χ. Since power-law couplings cannot be exactly described using the MPS method, we approximate the Hamiltonian by a sum of exponential terms as [63]

$$\frac{1}{|i-j|^\alpha} = \sum_{n}^{N_e} f_n e^{-\lambda_n |i-j|}, \tag{15}$$

which can be represented efficiently as a matrix product operator. By default, we approximate power-law couplings using a sum of N_e exponential functions. These functions are fitted within a range of $L-1$ sites to ensure the resulting approximated couplings deviate from the exact values by less than 2% for any pair of sites [20].

We use the maximum bond dimension $\chi_{\max} = 512$ (we check its convergence in Appendix A), sampling number $N_s = 40$, and time step $\delta t = 0.01$ as typical parameters in TDVP calculations. Equation (13) is evaluated completely using the TDVP algorithm with the total magnetization conserved in the open-source library TenPy [82]. In detail, we use a hybrid variation of the TDVP scheme [83,84], where we first use a two-site version of TDVP to dynamically grow the bond dimension to its maximum $\chi_{\max}$ and then shift to the one-site version to avoid any errors due to truncation in singular values that appears in the two-site version [85].

IV. RESULTS AND DISCUSSION

A. Perturbative short-time dynamics

At infinite temperature, i.e., $\beta = 0$, the trace in Eq. (3) can be expanded up to the second order of t at short times. In the Heisenberg picture, we have the expansion of $\sigma_j^z(t)$ as

$$\begin{aligned} \hat{\sigma}_j^z(t) &= e^{i\hat{H}t} \hat{\sigma}_j^z e^{-i\hat{H}t} \\ &= \hat{\sigma}_j^z + it\left[\hat{H}, \hat{\sigma}_j^z\right] + \frac{(it)^2}{2!}\left[\hat{H}, \left[\hat{H}, \hat{\sigma}_j^z\right]\right] + O(t^3). \end{aligned} \tag{16}$$

After evaluating the commutator, the second term in Eq. (16) reads

$$[\hat{H}, \hat{\sigma}_j^z] = -i \sum_{i \neq j} J_{ij} \left(\hat{\sigma}_i^x \hat{\sigma}_j^y - \hat{\sigma}_i^y \hat{\sigma}_j^x\right), \tag{17}$$

which is Δ-independent and acts as the spin-current operator. The third term of Eq. (16) has the following complicated form:

$$\begin{aligned} \left[\hat{H}, \left[\hat{H}, \hat{\sigma}_j^z\right]\right] = &\sum_{i\neq j}\sum_{k\neq j} J_{ij}J_{kj}\left(\hat{\sigma}_k^x\hat{\sigma}_i^x\hat{\sigma}_j^z + \hat{\sigma}_k^y\hat{\sigma}_i^y\hat{\sigma}_j^z\right) \\ &- \sum_{i\neq k}\sum_{k\neq j} J_{ik}J_{kj}\left(\hat{\sigma}_i^x\hat{\sigma}_j^x\hat{\sigma}_k^z + \hat{\sigma}_i^y\hat{\sigma}_j^y\hat{\sigma}_k^z\right) \\ &- \sum_{i<j}\sum_{k\neq j} J_{ij}J_{kj}\Delta\left(\hat{\sigma}_i^z\hat{\sigma}_k^x\hat{\sigma}_j^x + \hat{\sigma}_i^z\hat{\sigma}_k^y\hat{\sigma}_j^y\right) \\ &+ \sum_{i<k}\sum_{k\neq j} J_{ik}J_{kj}\Delta\left(\hat{\sigma}_i^z\hat{\sigma}_k^y\hat{\sigma}_j^y + \hat{\sigma}_i^z\hat{\sigma}_k^x\hat{\sigma}_j^x\right) \\ &- \sum_{j<i}\sum_{k\neq j} J_{ji}J_{kj}\Delta\left(\hat{\sigma}_k^x\hat{\sigma}_j^x\hat{\sigma}_i^z + \hat{\sigma}_k^y\hat{\sigma}_j^y\hat{\sigma}_i^z\right) \\ &+ \sum_{k<i}\sum_{k\neq j} J_{ki}J_{kj}\Delta\left(\hat{\sigma}_k^y\hat{\sigma}_j^y\hat{\sigma}_i^z + \hat{\sigma}_k^x\hat{\sigma}_j^x\hat{\sigma}_i^z\right), \end{aligned} \tag{18}$$

which explicitly depends on Δ. Furthermore, considering $\mathrm{Tr}[\hat{\sigma}_i^z\hat{\sigma}_j^z] = \delta_{ij}$ and $\mathrm{Tr}[\cdots\hat{\sigma}_i^{x(y)}\hat{\sigma}_j^{x(y)}\cdots]|_{i\neq j} = 0$, the unequal-time correlation function reads

$$C_j(t) \approx \begin{cases} 1 - t^2 \sum_{i\neq j} J_{ij}^2 & \text{for } j = 0, \\ t^2 J_{j0}^2 & \text{for } j \neq 0, \end{cases} \tag{19}$$

where $J_{ij} = -\mathcal{N}J/|i-j|^\alpha$ denotes the rescaled hopping strength.

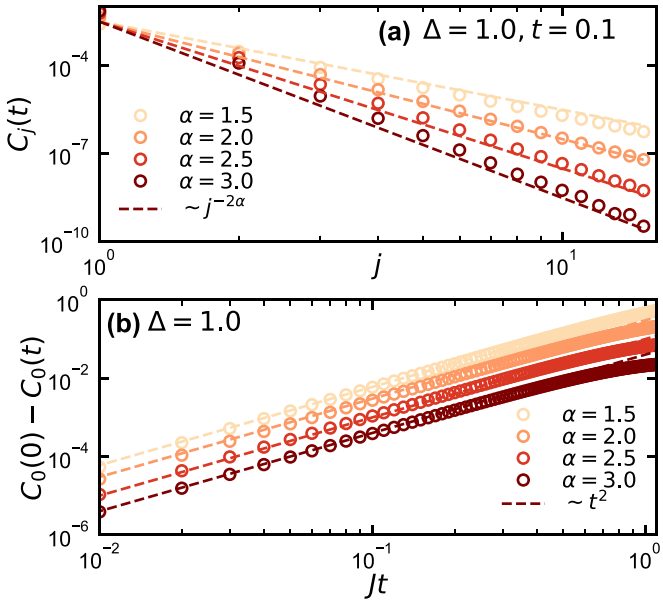

FIG. 2. (a) The profile of unequal-time correlation function at early time $t = 0.1$ for different α values is well fitted by power-law decay curves $j^{-2\alpha}$ (dashed lines) predicted by the perturbation theory. (b) Short-time dynamics of the autocorrelator for different α values which are fitted by quadratic curves t^2 (dashed lines). The numerical results are obtained by the TDVP simulation with a system size of $L = 27$.

The second-order perturbation theory yields a Δ-independent result. Remarkably, the autocorrelator exhibits quadratic decay early while the spatial correlation function at a fixed time inherits the algebraic decay at lattice distance j, falling off as $j^{-2\alpha}$. The short-time dynamics of the correlation function at $\Delta = 1.0$ for different α are shown in Fig. 2, where the spatially algebraic decay [Fig. 2(a)] and temporally quadratic decay [Fig. 2(b)] of the correlation function are both well captured by fitting lines. In other spin models without the Δ-dependent anisotropic term, due to the power-law spin exchange, the algebraic tails of the spatial correlation function are remarkable [2,19]. In our anisotropic model, we find that the algebraic tails cannot be suppressed by anisotropy Δ at early time. However, as we can see in the next section, the anisotropy Δ greatly influences the late-time hydrodynamics. This implies the interplay between anisotropy and long-range spin exchange.

B. Late-time hydrodynamics from autocorrelator

Beyond the perturbation theory, we now focus on the emergence of late-time hydrodynamic tails, falling off as $t^{-\gamma}$. At late times, the effect of anisotropy Δ is pronounced for anomalous transports. Expanding the trace in the energy eigenbasis $\hat{H}|n\rangle = E_n|n\rangle$, we have

$$C_j(t) = \sum_{n,m} \langle n|\hat{\sigma}_j^z|m\rangle\langle m|\hat{\sigma}_0^z|n\rangle e^{-i(E_n - E_m)t}. \tag{20}$$

The autocorrelator $C_0(t)$ consists of a superposition of $\cos[(E_n - E_m)t]$. The weight of each cosine function is determined by the matrix elements of $\hat{\sigma}^z$ in the energy basis. Such a form is reminiscent of the spectral form factor defined by $K(t) = \sum_{n,m} e^{-i(E_n - E_m)t}$. One may expect that $C_0(t)$ exhibits oscillations early, as seen in other spin models [18].

The autocorrelator $C_0(t)$ at $\Delta = 1.0$ and 0.5 for different α is demonstrated in Fig. 3. Early, typically $Jt < 1$, the autocorrelator presents rapid decay so that it reaches a local equilibrium. Afterward, the autocorrelator suddenly increases and exhibits slow hydrodynamic transport constrained by the conserved magnetization at an intermediate time. Eventually, the system enters a global equilibrium. More evidence of these multiple stages can also be found in the inset of Fig. 9 (see in Appendix B).

As expected, the power-law decay exists but is hindered by oscillations at late time ($t > 1$). This is similar to the imbalance dynamics in the presence of disorder. To extract the dynamical exponent γ, we find a proper fitting function to capture the relaxation at late time ($t > 1$) [86],

$$C_0(t) = ae^{-t/\tau}\cos(\beta t + \phi) + bt^{-\gamma}[1 + ct^{-\eta}\sin(\omega t + \phi)]. \tag{21}$$

The second term has a primary contribution and it consists of a primary algebraic tail $t^{-\gamma}$ and damped oscillation with specific frequency ω. For $\Delta = 1.0$, as α increases from 1.5 up to 3.0, we find that the dynamical exponent first increases until it reaches its maximum value of $\gamma \simeq 1$ at $\alpha = 2.0$, and then it dramatically decreases [see Figs. 3(a)–3(d)]. Since γ is always higher than 1/2, this nonmonotonic behavior of γ could be considered as a superdiffusive-ballistic-superdiffusive transition. Similar nonmonotonic behavior also exists at $\Delta = 0.5$ as shown in Figs. 3(e)–3(h). What differs is that ballistic transport occurs at $\alpha = 2.75$ for $\Delta = 0.5$, indicating that this transition boundary is highly related to both Δ and α. Also, we notice that subdiffusion ($\gamma < 1/2$) appears at $\alpha = 1.5$. This is anomalous since long-range couplings usually lead to fast transport. The finite-size effect is effectively excluded for larger system sizes (see in Appendix C). We attribute this anomaly to the interplay between anisotropy and long-range couplings, which is vital but indistinct. Also, recent studies suggest that the long-range XY model exhibits diffusion at $\alpha = 1.5$ [1,2]. Then it is not surprising that weak anisotropy tends to bound spins with parallel polarization and leads to subdiffusion. One might notice that the fitted dynamical exponents in the inset of Fig. 11(a) do not show strong convergence. We attribute this to the long-range couplings, which are hard to be accurately captured in the TDVP method. Thus, a more rigorous theoretical analysis is required to substantiate this point.

Then, based on the fitting from Eq. (21), we have the phase diagram of transport properties, i.e., the dynamical exponent γ as a function of Δ and α as shown in Fig. 1(a). There are three kinds of phase: subdiffusion ($\gamma < 1/2$), superdiffusion ($1/2 < \gamma < 1$), and ballistic transport ($\gamma \simeq 1$). Remarkably, an anomalous superdiffusive-ballistic-superdiffusive transition generally exists at an arbitrary anisotropy Δ. We find the peak value of such transitions can be greatly captured by an exponential fitting curve $\Delta \simeq e^{-\alpha+2}$ (red dashed curve). This anomalous hydrodynamics strongly violates the expected diffusion in a nonintegrable system, which is one of the highlights of our work.

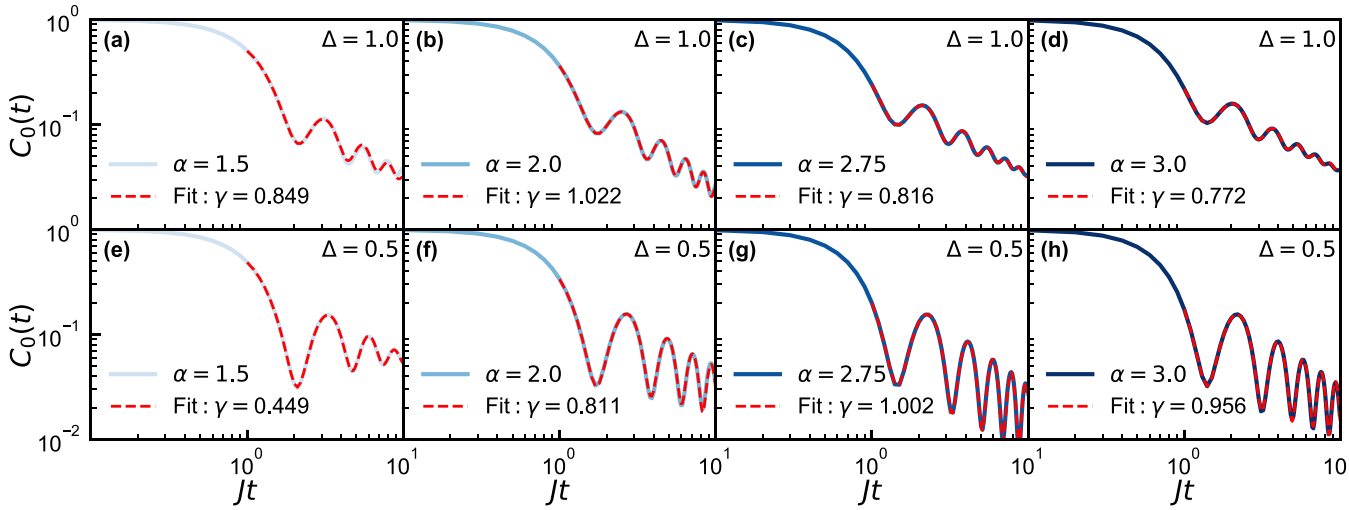

FIG. 3. The autocorrelator $C_0(t)$ at $\Delta = 1.0$ [(a)–(d)] and 0.5 [(e)–(h)] for different α values in the log-log scale. The system sizes are all $L = 21$ by using the DQT method. The red dashed lines denote the fitting function in Eq. (21).

Intuitively, such a nonmonotonic behavior of γ is induced by anisotropy Δ against long-range exponent α. It has been shown that strong anisotropy acts as an attractive potential to bound two spins with parallel polarization in the ferromagnetic phase ($\Delta > 0$), leading to bound states at large Δ [50,51]. Thus, the anisotropy can slow down the spreading of spins. On the contrary, long-range couplings tend to rapidly relax spins away from initial excitation. Then ballistic transport emerges when the effects of them are balanced. Since ballistic transport generally exists in integrable systems, our model at the transition point might be linked to some integrable models. In particular, we note that at $\Delta = 1.0$ and $\alpha = 2.0$, Eq. (1) in the thermodynamic limit corresponds to the well-known Haldane-Shastry integrable model [87,88].

C. Emergent region against quantum chaos

Typically, a quantum integrable system possesses an extensive set of conserved quantities, which prevent the system from quantum chaos and its information loss. These conserved quantities represent observables whose expectation values remain constant as the system evolves. As shown in the following section, the spin current operator $\hat{J}$ exhibits near-constant behavior during ballistic transport, indicating a corresponding conservation law in the Hamiltonian. Utilizing the random matrix theory (RMT), we find that the energy-level-spacing statistics of our Hamiltonian in the same parameter space (Δ, α) in Fig. 1(a) mostly obey the Wigner-Dyson distribution with a ratio $\langle r \rangle \approx 0.53$ [see in Figs. 4(b) and 4(d)]. For a larger system size, the regime of the level-spacing ratio around 0.53 becomes larger as shown in Fig. 4(d), which suggests the lack of ballistic transport. This indicates that this long-range spin system is nonintegrable, contradicting our previous understanding.

To further quantify the quantum chaos beyond the RMT, we investigate the microcanonical distributions of eigenstate entanglement entropy (EE) by following the recent Ref. [89]. For a chosen eigenstate $|\psi\rangle$, the von Neumann entanglement entropy of a subsystem A is defined as $S_A = -\mathrm{Tr}[\rho_A \ln \rho_A]$ with the reduced density matrix $\rho_A = \mathrm{Tr}_B[|\psi\rangle\langle\psi|]$. For a Hamiltonian system, the central idea amounts to comparing the subsystem's EE distribution $P_{\mathrm{E}}(S_A)$ of eigenstates at the midspectrum to the reference distribution of a pure random state, i.e., the Bianchi-Dona (BD) distribution $P_{\mathrm{BD}}(S_A)$. The distance between distributions is characterized by the Kullback-Leibler (KL) divergence D_{KL}. If we assume that $P_{\mathrm{E}}(S_A)$ and $P_{\mathrm{BD}}(S_A)$ are Gaussian distributions, the KL divergence is given by

$$D_{\mathrm{KL}} = \frac{(\mu_{\mathrm{E}} - \mu_{\mathrm{BD}})^2}{2\sigma_{\mathrm{BD}}^2} + \frac{1}{2}\left[\left(\frac{\sigma_{\mathrm{E}}}{\sigma_{\mathrm{BD}}}\right)^2 - 1\right] - \ln\frac{\sigma_{\mathrm{E}}}{\sigma_{\mathrm{BD}}}, \tag{22}$$

where μ and σ are the mean value and the standard deviation of EE distribution $P(S_A)$, respectively.

Then, we choose the typical system sizes as $L = 12$ and 14 with the subsystem size $L_A = L/2$ in the half-filling sector $\sum_i \hat{\sigma}_i^z = 0$. For $L = 12$, the mean and standard deviation of the BD distribution is $\mu_{\mathrm{BD}} \approx 3.5745$ and $\sigma_{\mathrm{BD}} \approx 0.0199$, respectively. For $L = 14$, $\mu_{\mathrm{BD}} \approx 4.2652$ and $\sigma_{\mathrm{BD}} \approx 0.0103$ [89]. We select 100 eigenstates ($L = 12$) and 300 eigenstates ($L = 14$), lying in a small energy window whose density of states (DOS) is the largest to compute the half-chain EE and the corresponding μ_{E} and σ_{E}. To further remove the fluctuations from sampling eigenstates, we add a weak disorder $h_i \sum_i \hat{\sigma}_i^z$ to Eq. (1) with h_i randomly drawn from $[-0.1J, 0.1J]$. The EE distribution is averaged over 100 disorder realizations for both $L = 12$ and 14, respectively. The divergence D_{KL} as a function of (Δ, α) is plotted in Fig. 1(b). Since our model at $\alpha \to \infty$ reduces to the integrable Heisenberg model, the divergence increases monotonically with increasing α. Surprisingly, for different values of Δ, a narrow region consistently emerges (shown in dark purple) where D_{KL} reaches a local maximum after resuming its monotonic rise. These unexpected local maxima defy the typical behavior associated with quantum chaos, even though the model is considered ergodic. Notably, unlike the level statistics, D_{KL} shows

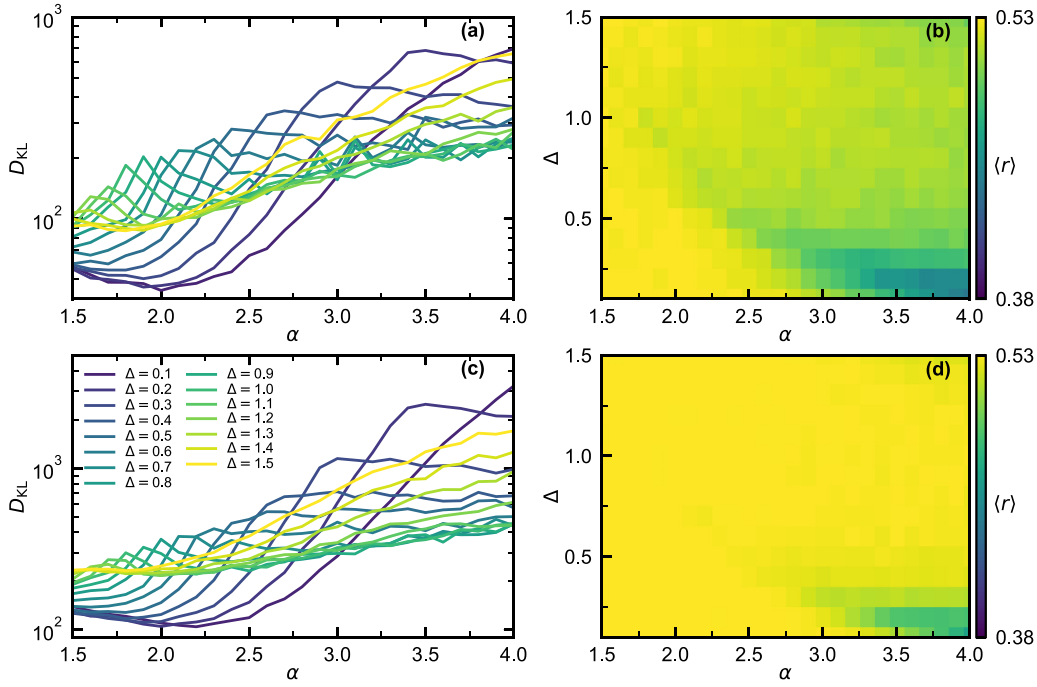

FIG. 4. (a) and (b): The Kullback-Leibler divergence (a) and the level-spacing ratio (b) for system size $L = 12$ at the half-filling condition. (c)–(d): The same data as in (a) and (b) for system size $L = 14$ at the half-filling condition.

less dependency on the system size and maintains the same behavior for a larger system size [see in Figs. 4(a) and 4(c)]. This indicates the robustness and sensitivity of KL divergence on quantifying how far a system is from quantum chaos, since eigenstates of local systems also encode structures beyond the RMT. Remarkably, the points (Δ, α) at which these maxima occur can all be described by the same exponential curve $\Delta \simeq e^{-\alpha+2}$ (red dashed curve) in Fig. 1(a). This suggests that our model exhibits an emergent property that resists quantum chaos at specific points (Δ, α) around this exponential fitting curve. This finding aligns with the anomalous ballistic transport in Fig. 1(a), which is the other highlight of our work.

D. Broadening of spin excitation

To further confirm this anomalous phenomenon, we now investigate the mean-square displacement (MSD). This quantity reflects the spread of spin excitation over space and time. Here, we focus on the isotropic case $\Delta = 1.0$ to quantitatively investigate the nonmonotonic behavior of γ with varying α. We can extract the diffusion coefficient $D(t) \propto t^{2\gamma-1}$ and dynamical exponent $\gamma(t)$ from Eq. (4). Diffusion coefficients for different values of α with different system sizes are shown in Figs. 5(a)–5(d). Note that the results of the DQT and TDVP methods agree with each other for all α in Figs. 5(a)–5(d). Increasing the system size does not halt the growth of $D(t)$ for all the considered values of α. This excludes diffusive transport since a diffusion process would exhibit a size-independent plateau [constant $D(t)$] at large system sizes. Moreover, we find that $D(t)$ grows rapidly and nearly linearly at $\alpha = 2.0$, then slows down at $\alpha = 1.5$. This nonmonotonic behavior of $D(t)$ reflects the transition again from superdiffusive to ballistic and then back to superdiffusive transport.

In Figs. 5(e)–5(h), we extract the time-dependent dynamical exponents $\gamma(t)$ for various values of α and system sizes. This allows us to quantitatively distinguish between different transports. In the ideal scenario, $\gamma(t)$ would converge at a finite value as time approaches infinity $\lim_{t\to\infty} \gamma(t) \approx \gamma$. For a finite system, the plateau in $\gamma(t)$ is short lived. However, as the system size increases, $\gamma(t)$ gradually converges to a stable curve for all the considered values of α. We also find that the dynamical exponent in Figs. 5(e)–5(h) is always larger than $1/2$, indicating the absence of diffusion. Remarkably, $\gamma(t)$ is quite close to 1 at $\alpha = 2.0$ where we believe ballistic transport occurs. The ballistic transport at $\alpha = 2.0$ is further verified by the spatial correlation function in Fig. 10 (see in Appendix B). Interestingly, the density profile at the central part of the chain is different from the Gaussian fitting curves (dashed curves in Fig. 10). This indicates that the transport mechanism is beyond the diffusion. The values of $\gamma(t)$ for other α are smaller than 1 and this implies a nonmonotonic change in transport behavior. Figure 6 summarizes the dynamical exponent γ as a function of some typical values of α for different system sizes. The stable dynamical exponents, represented by γ, are obtained by averaging over the stable plateaus in Figs. 5(e)–5(h). As expected, the nonmonotonic behavior of γ persists for various system sizes, with ballistic transport occurring around $\alpha = 2.0$.

E. Understanding from the Kubo formula

Linear response theory provides a universal framework for understanding a system's response to an external force treated as a perturbation. It allows us to understand this

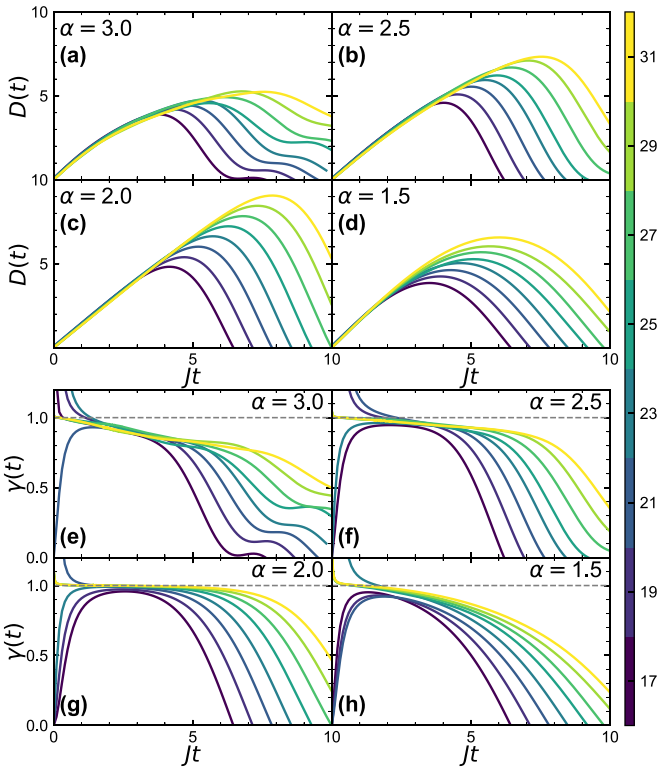

FIG. 5. Diffusion coefficient $D(t)$ for $\alpha = 3.0$ (a), 2.5 (b), 2.0 (c), 1.5 (d) with different system sizes. Dynamical exponent $\gamma(t)$ for $\alpha = 3.0$ (e), 2.5 (f), 2.0 (g), 1.5 (h) with different system sizes. We utilize the DQT method for $L = 17, 19, 21, 23$ and the TDVP technique for $L = 25, 27, 29, 31$.

superdiffusive-ballistic-superdiffusive transition in the frequency domain. Thus, the transport behavior can be characterized by the spin conductivity $\sigma(\omega)$, which

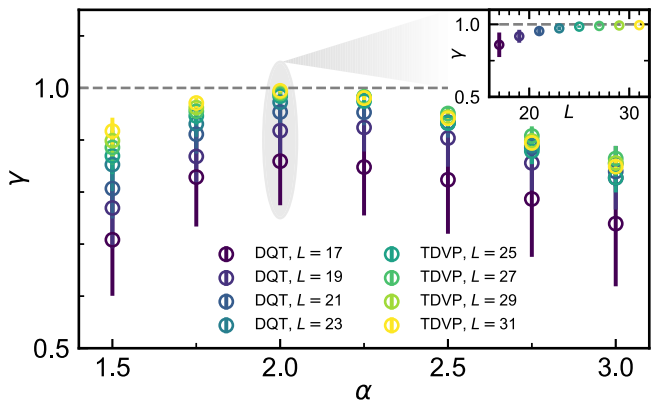

FIG. 6. Dynamical exponent γ as a function of α for different system sizes. Dynamical exponent γ is obtained by averaging $\gamma(t)$ over the time window of $Jt \in [3, 5]$. The error bars denote the standard deviation of γ. The dashed line denotes the ballistic transport ($\gamma = 1$). The inset shows the dynamical exponent γ at $\alpha = 2.0$ as a function of the system size L. One can see that γ gradually converges with increasing L.

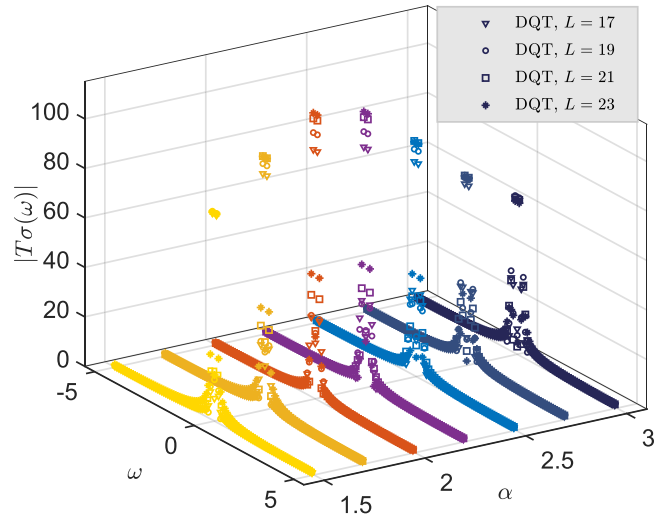

FIG. 7. The spin conductivity $|T\sigma(\omega)|$ at $\Delta = 1.0$ for different α values and different system sizes.

reads [11,12]

$$T\sigma(\omega) = \frac{1}{L}\int_0^\infty dt\,\langle \hat{J}(t)\hat{J}(0)\rangle e^{i\omega t}, \tag{23}$$

where the current operator $\hat{J} = \sum_l \hat{J}_l$ is defined by the lattice continuity equation $\partial_t \hat{\sigma}_l^z = i[\hat{H}, \hat{\sigma}_l^z] = \hat{J}_{l-1} - \hat{J}_l$. Note that $T\sigma(\omega)$ has a finite value since $\sigma(\omega) \to 0$ at infinite temperature limit $T \to \infty$, implying that the system does not respond to any perturbations. Its continuous form leads to a generalized relation as [90,91]

$$\frac{1}{2}\frac{d^2}{dt^2}\Sigma^2(t) = \frac{1}{L}\langle \hat{J}(t)\hat{J}(0)\rangle. \tag{24}$$

Then, substituting Eq. (24) into Eq. (23) and taking $\Sigma^2(t) \sim t^{2\gamma}$, we have

$$T\sigma'(\omega) \sim \omega^{1-2\gamma}, \tag{25}$$

where $\sigma'(\omega)$ is the real part of $\sigma(\omega)$. This means that the static response diverges when transports are ballistic or superdiffusive (i.e., $1/2 < \gamma \leqslant 1$). Then we can decompose $\sigma'(\omega)$ into a singular and a regular part [11]

$$T\sigma'(\omega) = TD_{\text{Drude}}\delta(\omega) + T\sigma_{\text{reg}}(\omega), \tag{26}$$

where the D_{Drude} is the so-called Drude weight. Since the Drude weight trivially vanishes at $T \to \infty$, one can expect TD_{Drude} to be finite. Referring back to Eq. (23), this result signifies that the injected currents do not completely decay, i.e., ballistic transport in an ideal conductor. Notably, for systems with a finite local Hilbert space, the singularity in the conductivity cannot be stronger than ω^{-1} [11]. Consequently, a nonzero Drude conductivity ($TD_{\text{Drude}} \neq 0$) only occurs when the ballistic transport is present (i.e., $\gamma = 1$). In this case, this ω^{-1} term is included in the δ function of the Kubo formula, while weaker singularities are retained in the part of $\sigma_{\text{reg}}(\omega)$.

Here we focus on the divergence of $|T\sigma(\omega = 0)|$ instead of giving the exact value of TD_{Drude}. We show the absolute value of conductivity for typical α values and different system sizes in Fig. 7, where $T\sigma(\omega)$ is obtained from the Fourier

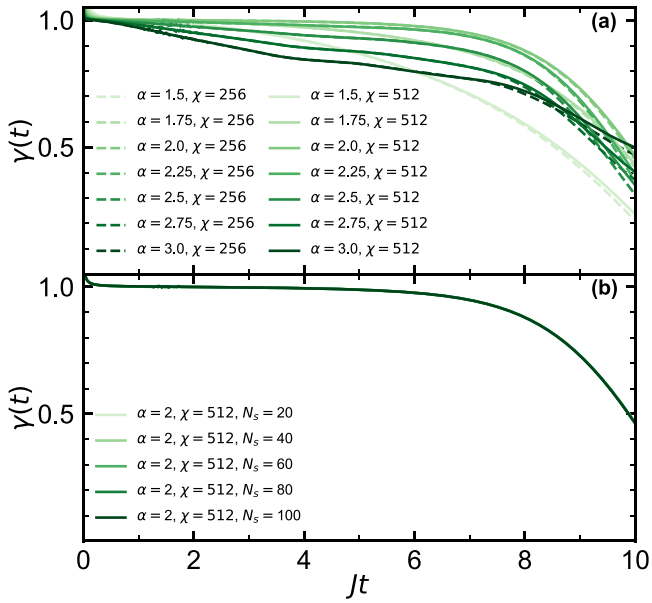

FIG. 8. (a) Time-dependent dynamical exponent $\gamma(t)$ for different α values and bond dimensions χ. The number of random state samples is $N_s = 40$. (b) Time-dependent dynamical exponent $\gamma(t)$ at $\alpha = 2.0$ for different samples $N = 20, 40, 60, 80, 100$. The bond dimension is $\chi = 512$ and the system size in both (a) and (b) is $L = 31$ for TDVP simulations.

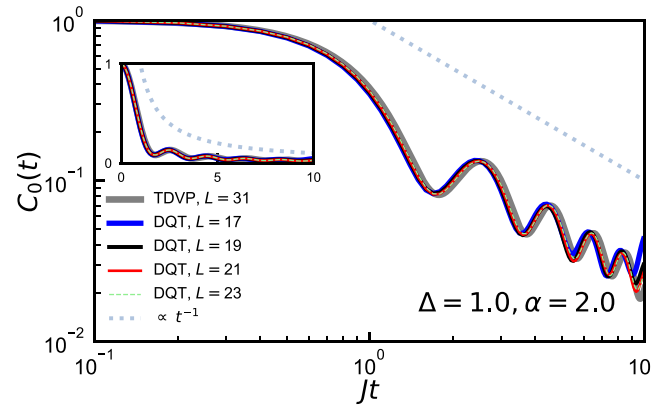

FIG. 9. Autocorrelators $C_0(t)$ for $\alpha = 2.0$ and $\Delta = 1.0$ with system sizes $L = 17, 19, 21, 23$ (DQT), 31 (TDVP) in the log-log scale. The light steel blue dashed line indicates ballistic transport $\propto t^{-1}$. The inset shows the same quantities but on a linear scale.

transform of Eq. (24). As expected, all conductivities become increasingly peaked around $\omega = 0$, indicating that $\gamma > 1/2$. Moreover, as α increases, the peak becomes higher and it reaches a maximum value at $\alpha = 2.0$ followed by a decrease. This nonmonotonic behavior generally exists independent of system sizes. $T\sigma(0)$ at $\alpha = 2.0$ has the largest singularity, indicating the existence of ballistic transport, and agrees with the MSD analysis above. One can also find that, for $\gamma = 1$, the current-current correlator $\langle \hat{J}(t)\hat{J}(0)\rangle$ is a constant, implying that the current operator $\hat{J}$ commutes with the Hamiltonian. This is manifested on the emergent local maximum of D_{KL}.

V. CONCLUSION

In summary, we have employed both DQT and TDVP approaches to numerically study the unequal-time spin-spin correlations at infinite temperature in a long-range spin-1/2 XXZ model. By varying the long-range exponent α, we find an anomalous superdiffusive-ballistic-superdiffusive transition for all anisotropy values in $\Delta \in (0, 1.5]$. This phenomenon is also supported by the static spin conductivity $T\sigma(\omega = 0)$, which exhibits the largest singularity in the presence of ballistic transport. Moreover, the boundary of this transition can be well fitted by an exponential curve $\Delta \simeq e^{-\alpha+2}$. This transition is caused by the interplay between anisotropy and long-range couplings. We further investigate the Kullback-Leibler divergence between the entanglement entropy's microcanonical distribution of eigenstates and that of a purely random state. This analysis suggests that the ergodic long-range XXZ model exhibits resistance to quantum chaos at the transition boundary. Interestingly, similar signatures could be present in anomalous hydrodynamic behaviors in other nonintegrable quantum many-body systems. Since these transports occur at high temperatures, it would be useful to study the classical description of spin density relaxation in the long-range XXZ model. However, understanding the mechanism behind this ballistic transport and its connection to the emergent resistance to quantum chaos in nonintegrable quantum systems remains an open question.

We study the magnetization dynamics above in a restricted range of anisotropy Δ and long-range exponent α. By expanding these parameter ranges, the system can exhibit various types of transport behavior for spin relaxation, including subdiffusive, diffusive, superdiffusive, and ballistic. We expect there to be optimal points where standard diffusion and KPZ superdiffusion become dominant. Our work focuses on the infinite-temperature limit, involving the entire Hilbert space. This approach also allows us to measure the autocorrelator by averaging over product states, which aligns with how hydrodynamics are observed in experiments. Although recent work has utilized quantum circuits to directly measure the infinite-temperature autocorrelator without needing to sample product states [34], our study offers the advantage of being readily adaptable to finite-temperature regimes, where spin relaxation might be slower.

ACKNOWLEDGMENTS

We thank Dr. Dario Poletti for helpful discussions. This work was supported by the National Natural Science Foundation of China under Grant No. 12375021 and the National Key R&D Program of China under Grant No. 2022YFA1404203.

APPENDIX A: CONVERGENCE OF TDVP RESULTS WITH BOND DIMENSION AND RANDOM STATE SAMPLES

Here we briefly show that the dynamical exponent $\gamma(t)$ obtained by the TDVP method is converged with bond dimen-

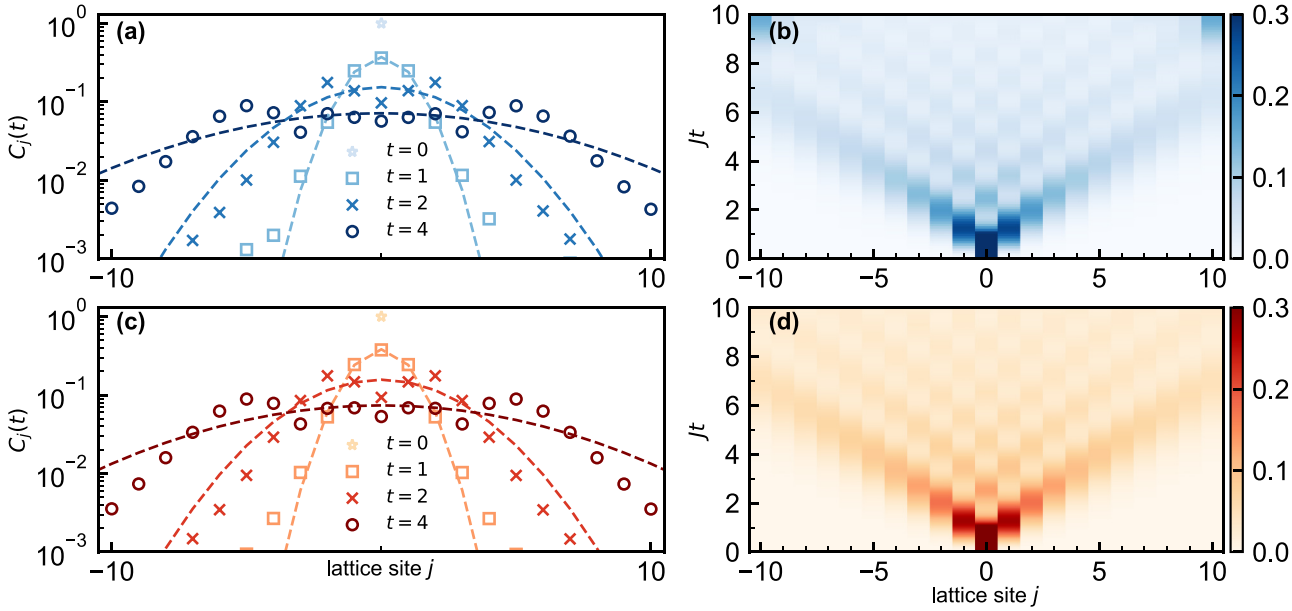

FIG. 10. (a) and (b): Density profiles for $\alpha = 2.0$ and $\Delta = 1.0$ with $L = 23$ (DQT) (a) and the corresponding broadening of spin excitation (b). (c) and (d): The same data with $L = 31$ (TDVP). Dashed curves are Gaussian fits to the data in (a) and (c).

sion and samples. We focus on the isotropic case $\Delta = 1.0$. As shown in Fig. 8(a), despite different α, $\gamma(t)$ are all converged for a long time ($Jt \approx 8$) with increasing bond dimension. The flat part of $\gamma(t)$ is reliable for extracting a stable dynamical exponent γ. Besides, ballistic transport is expected to occur at $\alpha = 2.0$; hence we try different sampling numbers of random states to check the result. With fixed χ and increasing samples up to $N = 100$ in Fig. 8(b), $\gamma(t)$ perfectly converges. We have checked that $\gamma(t)$ for other α is also converged with sampling numbers, and $N_s = 40$ is enough for TDVP calculation.

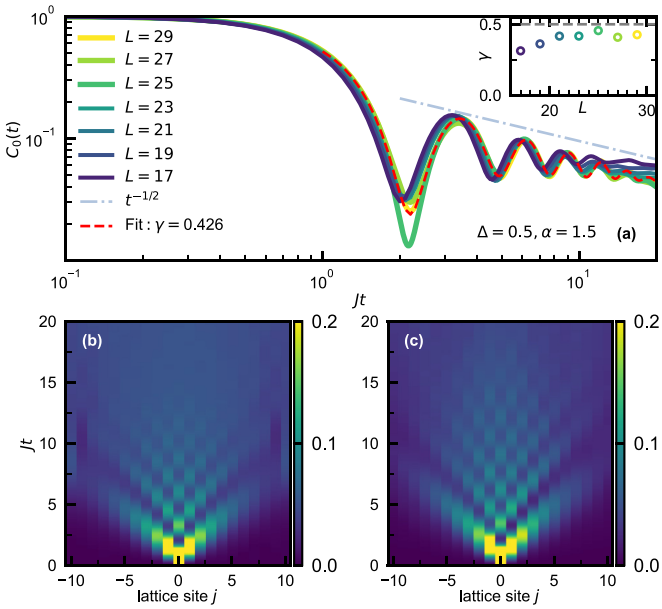

FIG. 11. The spin-spin correlator $C_j(t)$ at $(\Delta, \alpha) = (0.5, 1.5)$ for different system sizes ranging from $L = 17$ up to $L = 29$. DQT method is used for $L = 17, 19, 21, 23$ and TDVP method is used for $L = 25, 27, 29$. (a) The autocorrelator $C_0(t)$ for different system sizes. The red dashed line denotes the fitting to $C_0(t)$ for $L = 29$. The inset shows the extracted dynamical exponent γ as a function of the system size L. (b) and (c): The spatial and temporal expansions of the correlator for $L = 21$ (b) and $L = 29$ (c).

APPENDIX B: COMPARISON OF DQT AND TDVP RESULTS

To verify the accuracy of the TDVP method, we briefly compare the autocorrelator and broadening of spin density obtained from DQT and TDVP methods. Figure 9 shows the autocorrelators with different system sizes at $\alpha = 2.0$ and $\Delta = 1.0$ where ballistic transport is present. One finds that as the system size increases, different autocorrelators gradually converge to a stable curve. This curve roughly matches the ballistic decay. Besides, benefiting from the large system size, the TDVP method efficiently improves the boundary effect [see Figs. 10(b) and 10(d)]. The density profiles obtained from the two methods are also in good agreement at the intermediate timescale.

APPENDIX C: FINITE-SIZE ANALYSIS FOR ANOMALOUS SUBDIFFUSION

To exclude the finite-size effect, we calculate the spin-spin correlators at a typical parameter $(\Delta, \alpha) = (0.5, 1.5)$ for larger system sizes. As shown in Fig. 11(a) and inset, the autocorrelator gradually converges with increasing the system size ranging from $L = 17$ up to $L = 29$. The light blue dashed line denotes the standard diffusion, showing similarity

to the decay behavior of the autocorrelators. But more detailed fitting (red dashed line) to the autocorrelator for $L = 29$ still gives a subdiffusive dynamical exponent $\gamma < 1/2$. The profile expansions for $L = 21$ and 29 are also shown in Figs. 11(b) and 11(c). One can see a clear boundary reflection at $Jt \approx 10$ in Fig. 11(b). Yet such a finite-size effect is effectively excluded for a larger system size in Fig. 11(c). Our result suggests the existence of subdiffusion for weak anisotropies and long-range couplings.

APPENDIX D: LEVEL STATISTICS AND THE KL DIVERGENCE

By using exact diagonalization, we compute the consecutive energy gaps $\delta_k = E_{k+1} - E_k$ of the Hamiltonian. The level statistics are characterized by their ratio $r_k = \min(\delta_{k+1}, \delta k)/\max(\delta_{k+1}, \delta k)$. The averaged value $\langle r \rangle$ allows one to distinguish between the Poisson and Wigner-Dyson level statistics. The ergodic phase is known to follow the Wigner-Dyson distribution with $\langle r \rangle \approx 0.53$. In Figs. 4(b) and 4(d), we illustrate the ratios $\langle r \rangle$ for all (Δ, α) considered here, which mostly fluctuate around 0.53, indicating that the system is ergodic.

The Kullback-Leibler (KL) divergence between distributions $P_{\mathrm{E}}(S_A)$ and $P_{\mathrm{BD}}(S_A)$ is defined as

$$D_{\mathrm{KL}}(P_{\mathrm{E}}, P_{\mathrm{BD}}) = \int dS_A P_{\mathrm{E}}(S_A) \ln \frac{P_{\mathrm{E}}(S_A)}{P_{\mathrm{BD}}(S_A)}. \tag{D1}$$

To simply evaluate Eq. (D1), we directly calculate the mean value μ and the standard deviation σ of the entanglement entropy distribution $P(S_A)$, which is approximated by a Gaussian distribution as [89] $P(S_A) \approx \frac{1}{\sqrt{2\pi\sigma^2}} \exp[-\frac{(S_A-\mu)^2}{2\sigma^2}]$. Thus, D_{KL} can be evaluated by Eq. (22). The local maximum of D_{KL} for different Δ is shown in Figs. 4(a) and 4(c). One finds that the emergent local maximums are robust with increasing system size.

[1] M. K. Joshi, F. Kranzl, A. Schuckert, I. Lovas, C. Maier, R. Blatt, M. Knap, and C. F. Roos, Science **376**, 720 (2022).
[2] A. Schuckert, I. Lovas, and M. Knap, Phys. Rev. B **101**, 020416(R) (2020).
[3] D. Wei, A. Rubio-Abadal, B. Ye, F. Machado, J. Kemp, K. Srakaew, S. Hollerith, J. Rui, S. Gopalakrishnan, N. Y. Yao, I. Bloch, and J. Zeiher, Science **376**, 716 (2022).
[4] M. Ljubotina, M. Žnidarič, and T. Prosen, Phys. Rev. Lett. **122**, 210602 (2019).
[5] M. Dupont and J. E. Moore, Phys. Rev. B **101**, 121106(R) (2020).
[6] R. Steinigeweg, J. Gemmer, and W. Brenig, Phys. Rev. B **91**, 104404 (2015).
[7] B. Ye, F. Machado, C. D. White, R. S. K. Mong, and N. Y. Yao, Phys. Rev. Lett. **125**, 030601 (2020).
[8] J. Lux, J. Müller, A. Mitra, and A. Rosch, Phys. Rev. A **89**, 053608 (2014).
[9] V. B. Bulchandani, S. Gopalakrishnan, and E. Ilievski, J. Stat. Mech.: Theory Exp. (2021) 084001.
[10] J. W. Bush and A. U. Oza, Rep. Prog. Phys. **84**, 017001 (2020).
[11] B. Bertini, F. Heidrich-Meisner, C. Karrasch, T. Prosen, R. Steinigeweg, and M. Žnidarič, Rev. Mod. Phys. **93**, 025003 (2021).
[12] S. Gopalakrishnan and R. Vasseur, Rep. Prog. Phys. **86**, 036502 (2023).
[13] J. Feldmeier, P. Sala, G. De Tomasi, F. Pollmann, and M. Knap, Phys. Rev. Lett. **125**, 245303 (2020).
[14] A. J. McRoberts, T. Bilitewski, M. Haque, and R. Moessner, Phys. Rev. B **105**, L100403 (2022).
[15] R. Menu and T. Roscilde, Phys. Rev. Lett. **124**, 130604 (2020).
[16] J. Richter and A. Pal, Phys. Rev. Res. **4**, L012003 (2022).
[17] X. Zotos, Phys. Rev. Lett. **82**, 1764 (1999).
[18] J. Richter, N. Casper, W. Brenig, and R. Steinigeweg, Phys. Rev. B **100**, 144423 (2019).
[19] B. Kloss and Y. Bar Lev, Phys. Rev. A **99**, 032114 (2019).
[20] B. Kloss and Y. Bar Lev, Phys. Rev. B **102**, 060201(R) (2020).
[21] M. Brenes, E. Mascarenhas, M. Rigol, and J. Goold, Phys. Rev. B **98**, 235128 (2018).
[22] C. Gross and I. Bloch, Science **357**, 995 (2017).
[23] S. Hild, T. Fukuhara, P. Schauß, J. Zeiher, M. Knap, E. Demler, I. Bloch, and C. Gross, Phys. Rev. Lett. **113**, 147205 (2014).
[24] P. N. Jepsen, J. Amato-Grill, I. Dimitrova, W. W. Ho, E. Demler, and W. Ketterle, Nature (London) **588**, 403 (2020).
[25] F. Schäfer, T. Fukuhara, S. Sugawa, Y. Takasu, and Y. Takahashi, Nat. Rev. Phys. **2**, 411 (2020).
[26] J. Zhang, G. Pagano, P. W. Hess, A. Kyprianidis, P. Becker, H. Kaplan, A. V. Gorshkov, Z.-X. Gong, and C. Monroe, Nature (London) **551**, 601 (2017).
[27] S. E. Anderson, K. C. Younge, and G. Raithel, Phys. Rev. Lett. **107**, 263001 (2011).
[28] A. Browaeys and T. Lahaye, Nat. Phys. **16**, 132 (2020).
[29] S. Geier, N. Thaicharoen, C. Hainaut, T. Franz, A. Salzinger, A. Tebben, D. Grimshandl, G. Zürn, and M. Weidemüller, Science **374**, 1149 (2021).
[30] E. Guardado-Sanchez, P. T. Brown, D. Mitra, T. Devakul, D. A. Huse, P. Schauß, and W. S. Bakr, Phys. Rev. X **8**, 021069 (2018).
[31] S. Hollerith, K. Srakaew, D. Wei, A. Rubio-Abadal, D. Adler, P. Weckesser, A. Kruckenhauser, V. Walther, R. van Bijnen, J. Rui, C. Gross, I. Bloch, and J. Zeiher, Phys. Rev. Lett. **128**, 113602 (2022).
[32] H. Labuhn, D. Barredo, S. Ravets, S. De Léséleuc, T. Macrì, T. Lahaye, and A. Browaeys, Nature (London) **534**, 667 (2016).
[33] H. Weimer, M. Müller, I. Lesanovsky, P. Zoller, and H. P. Büchler, Nat. Phys. **6**, 382 (2010).
[34] Y.-H. Shi, Z.-H. Sun, Y.-Y. Wang, Z.-A. Wang, Y.-R. Zhang, W.-G. Ma, H.-T. Liu, K. Zhao, J.-C. Song, G.-H. Liang *et al.*, arXiv:2310.06565.
[35] R. Blatt and C. F. Roos, Nat. Phys. **8**, 277 (2012).
[36] R. Islam, E. Edwards, K. Kim, S. Korenblit, C. Noh, H. Carmichael, G.-D. Lin, L.-M. Duan, C.-C. Joseph Wang, J. Freericks *et al.*, Nat. Commun. **2**, 377 (2011).
[37] B. P. Lanyon, C. Hempel, D. Nigg, M. Müller, R. Gerritsma, F. Zähringer, P. Schindler, J. T. Barreiro, M. Rambach, G. Kirchmair *et al.*, Science **334**, 57 (2011).

[38] C. Schneider, D. Porras, and T. Schaetz, Rep. Prog. Phys. **75**, 024401 (2012).
[39] R. Steinigeweg, F. Jin, D. Schmidtke, H. De Raedt, K. Michielsen, and J. Gemmer, Phys. Rev. B **95**, 035155 (2017).
[40] J. Richter, F. Jin, L. Knipschild, J. Herbrych, H. De Raedt, K. Michielsen, J. Gemmer, and R. Steinigeweg, Phys. Rev. B **99**, 144422 (2019).
[41] M. Žnidarič, Phys. Rev. Lett. **110**, 070602 (2013).
[42] K. Aikawa, A. Frisch, M. Mark, S. Baier, A. Rietzler, R. Grimm, and F. Ferlaino, Phys. Rev. Lett. **108**, 210401 (2012).
[43] M. Lu, N. Q. Burdick, and B. L. Lev, Phys. Rev. Lett. **108**, 215301 (2012).
[44] P. Schauß, M. Cheneau, M. Endres, T. Fukuhara, S. Hild, A. Omran, T. Pohl, C. Gross, S. Kuhr, and I. Bloch, Nature (London) **491**, 87 (2012).
[45] M. Saffman, T. G. Walker, and K. Mølmer, Rev. Mod. Phys. **82**, 2313 (2010).
[46] B. Yan, S. A. Moses, B. Gadway, J. P. Covey, K. R. Hazzard, A. M. Rey, D. S. Jin, and J. Ye, Nature (London) **501**, 521 (2013).
[47] A. L. Burin, Phys. Rev. B **92**, 104428 (2015).
[48] A. Safavi-Naini, M. L. Wall, O. L. Acevedo, A. M. Rey, and R. M. Nandkishore, Phys. Rev. A **99**, 033610 (2019).
[49] S. Schiffer, J. Wang, X.-J. Liu, and H. Hu, Phys. Rev. A **100**, 063619 (2019).
[50] F. Kranzl, S. Birnkammer, M. K. Joshi, A. Bastianello, R. Blatt, M. Knap, and C. F. Roos, Phys. Rev. X **13**, 031017 (2023).
[51] T. Macrì, L. Lepori, G. Pagano, M. Lewenstein, and L. Barbiero, Phys. Rev. B **104**, 214309 (2021).
[52] S. Birnkammer, A. Bohrdt, F. Grusdt, and M. Knap, Phys. Rev. B **105**, L241103 (2022).
[53] L. Cevolani, J. Despres, G. Carleo, L. Tagliacozzo, and L. Sanchez-Palencia, Phys. Rev. B **98**, 024302 (2018).
[54] M. Foss-Feig, Z.-X. Gong, C. W. Clark, and A. V. Gorshkov, Phys. Rev. Lett. **114**, 157201 (2015).
[55] P. Hauke and L. Tagliacozzo, Phys. Rev. Lett. **111**, 207202 (2013).
[56] A. Lerose, B. Žunkovič, A. Silva, and A. Gambassi, Phys. Rev. B **99**, 121112(R) (2019).
[57] M. F. Maghrebi, Z.-X. Gong, M. Foss-Feig, and A. V. Gorshkov, Phys. Rev. B **93**, 125128 (2016).
[58] J. Ren, W.-L. You, and X. Wang, Phys. Rev. B **101**, 094410 (2020).
[59] L. Vanderstraeten, M. Van Damme, H. P. Büchler, and F. Verstraete, Phys. Rev. Lett. **121**, 090603 (2018).
[60] I. Frérot, P. Naldesi, and T. Roscilde, Phys. Rev. B **95**, 245111 (2017).
[61] V. Zaburdaev, S. Denisov, and J. Klafter, Rev. Mod. Phys. **87**, 483 (2015).
[62] M. Mierzejewski, J. Wronowicz, J. Pawłowski, and J. Herbrych, Phys. Rev. B **107**, 045134 (2023).
[63] K. Bull, A. Hallam, Z. Papić, and I. Martin, Phys. Rev. Lett. **129**, 140602 (2022).
[64] T. Heitmann, J. Richter, D. Schubert, and R. Steinigeweg, Z. Naturforsch., A: Phys. Sci. **75**, 421 (2020).
[65] F. Jin, D. Willsch, M. Willsch, H. Lagemann, K. Michielsen, and H. De Raedt, J. Phys. Soc. Jpn. **90**, 012001 (2021).
[66] J. Richter, F. Jin, H. De Raedt, K. Michielsen, J. Gemmer, and R. Steinigeweg, Phys. Rev. B **97**, 174430 (2018).
[67] M. Srednicki, Phys. Rev. E **50**, 888 (1994).
[68] J. M. Deutsch, Phys. Rev. A **43**, 2046 (1991).
[69] T. A. Elsayed and B. V. Fine, Phys. Rev. Lett. **110**, 070404 (2013).
[70] R. Steinigeweg, J. Gemmer, and W. Brenig, Phys. Rev. Lett. **112**, 120601 (2014).
[71] C. Bartsch and J. Gemmer, Phys. Rev. Lett. **102**, 110403 (2009).
[72] R. Steinigeweg, A. Khodja, H. Niemeyer, C. Gogolin, and J. Gemmer, Phys. Rev. Lett. **112**, 130403 (2014).
[73] S. Sugiura and A. Shimizu, Phys. Rev. Lett. **111**, 010401 (2013).
[74] T. Iitaka and T. Ebisuzaki, Phys. Rev. E **69**, 057701 (2004).
[75] L. Vidmar and M. Rigol, Phys. Rev. Lett. **119**, 220603 (2017).
[76] P. Weinberg and M. Bukov, SciPost Phys. **2**, 003 (2017).
[77] J. Haegeman, J. I. Cirac, T. J. Osborne, I. Pižorn, H. Verschelde, and F. Verstraete, Phys. Rev. Lett. **107**, 070601 (2011).
[78] J. Haegeman, T. J. Osborne, and F. Verstraete, Phys. Rev. B **88**, 075133 (2013).
[79] J. Haegeman, C. Lubich, I. Oseledets, B. Vandereycken, and F. Verstraete, Phys. Rev. B **94**, 165116 (2016).
[80] A. Wietek and A. M. Läuchli, Phys. Rev. E **98**, 033309 (2018).
[81] H. Kim and D. A. Huse, Phys. Rev. Lett. **111**, 127205 (2013).
[82] J. Hauschild and F. Pollmann, SciPost Phys. Lect. Notes 5 (2018).
[83] T. Chanda, R. Yao, and J. Zakrzewski, Phys. Rev. Res. **2**, 032039(R) (2020).
[84] T. Chanda, J. Zakrzewski, M. Lewenstein, and L. Tagliacozzo, Phys. Rev. Lett. **124**, 180602 (2020).
[85] S. Goto and I. Danshita, Phys. Rev. B **99**, 054307 (2019).
[86] D. J. Luitz, N. Laflorencie, and F. Alet, Phys. Rev. B **93**, 060201(R) (2016).
[87] F. D. M. Haldane, Phys. Rev. Lett. **60**, 635 (1988).
[88] B. S. Shastry, Phys. Rev. Lett. **60**, 639 (1988).
[89] J. F. Rodriguez-Nieva, C. Jonay, and V. Khemani, arXiv:2305.11940.
[90] J. D. Nardis, D. Bernard, and B. Doyon, SciPost Phys. **6**, 049 (2019).
[91] H. Singh, R. Vasseur, and S. Gopalakrishnan, Phys. Rev. Lett. **130**, 046001 (2023).